Impact of silver incorporation at the back contact of Kesterite solar cells on structural and device properties

Lwitiko P. Mwakyusa[a,b,*,#], Lennart Leist[a], Monika Rinke[c], Alexander Welle[d], Ulrich W. Paetzold[b,e], Bryce S. Richards[b,e], Michael Hetterich[a,e]

[a] *Institute of Applied Physics (APH), Karlsruhe Institute of Technology (KIT), 76131 Karlsruhe, Germany*
[b] *Institute of Microstructure Technology (IMT), KIT, 76344 Eggenstein-Leopoldshafen, Germany*
[c] *Institute for Applied Materials (IAM-AWP), KIT, 76344 Eggenstein-Leopoldshafen, Germany*
[d] *Institute of Functional Interfaces (IFG), KIT, 76344 Eggenstein-Leopoldshafen, Germany*
[e] *Light Technology Institute (LTI), KIT, 76131 Karlsruhe, Germany*

ARTICLE INFO

ABSTRACT

In the development of kesterite copper zinc tin selenide (CZTSe) thin-film solar cells, the realization of absorber layers with large grains and suppression of unwanted secondary phases have always been important aspects. Incorporation of silver (Ag) in the CZTSe absorber can improve grain growth but also affects both the bulk and interface electronic properties. In this work, the Ag layer was incorporated at the back contact of vacuum-processed CZTSe solar cells and its impact on the absorber growth and overall device performance was investigated. The concentration of Ag in the absorber was varied by changing the thickness of the Ag layer at the bottom of the copper-zinc-tin (CZT) precursor. We found that the grain size in the absorber significantly increased with increasing Ag layer thickness. We further investigated the phase and morphology evolution during annealing of the CZT precursor in selenium atmosphere, both with and without the Ag layer present. Using X-ray diffraction, Raman spectroscopy, and scanning electron microscopy, we demonstrated that Ag incorporation induced a fast formation of larger grains in the early stages, which could be attributed to the formation of a silver selenide (Ag–Se) liquid phase. Time-of-flight secondary ion mass spectrometry depth profiles revealed a homogeneous distribution of Ag across the absorber. An improved power conversion efficiency was obtained for very thin (10 nm) Ag layers – due to an increase in the open-circuit voltage and fill-factor – while thicker layers deteriorate the device properties, mainly due to an increased series resistance. Therefore, the incorporation of small amounts of Ag is suggested to be useful to improve the absorber morphology of CZTSe solar cells while the electronic properties suffer from too high quantities.

1. Introduction

Kesterite copper zinc tin (sulfo) selenide (CZT(S)Se) is a promising absorber material system for thin film solar cells since it only comprises earth abundant and low toxicity elements. Furthermore, it exhibits both a high absorption coefficient ($> 10^4$ cm^{-1}) and ideal bandgap energy (1.0 1.5 eV) for single junction photovoltaics (PV) [1]. However, despite these interesting properties, the power conversion efficiency (η) of CZTSe and CZTSSe cells still remains relatively low compared to other thin film PV technologies, with record values of 11.6 % (2019) [2] and 12.6 % (2014) [3], respectively, and little progress over the past five years. The limiting factors for the low η can mainly be traced back to a poor open circuit voltage (V_{OC}) and, partially, to a low

fill factor (*FF*). Many studies associated a poor V_{oc} with a large number of Cu$_{Zn}$ antisite defects, the presence of secondary phases, and small grain sizes of the absorber layer. The Cu$_{Zn}$ antisite defects were suggested to contribute to band tailing, which may contribute to the high V_{OC} deficit [1, 4, 5], although it could be shown that the latter is not significantly altered by varying the degree of Cu Zn disorder [6, 7]. Still, these defects may contribute significantly to the deterioration of device performance and should, therefore, be minimized. Theory suggests that partial substitution of Cu$^+$ or Zn^{2+} with an atom of different ionic radius could suppress the formation of these defects [4, 8 10]. Commonly, Ag$^+$ and Cd^{2+} are used to partially substitute Cu$^+$ and Zn^{2+}, respectively. Moreover, it was demonstrated that partial substitution of Cu$^+$ with Ag$^+$ can be used to tune the absorber bandgap

* Corresponding author.
  E-mail address: mwakyusa.lwitiko@udsm.ac.tz (L.P. Mwakyusa).
Present address: University of Dar es Salaam, Department of Physics, P.O.Box 35063, Dar es Salaam, Tanzania

Table 1
Selected publications describing Ag incorporation into the kesterite lattice.

Material	Process and precursor configuration	Annealing	η	Ref.
	Chemical			
CZTS	Spray pyrolysis (chalcogen-containing precursor)	S @ 600°C	7.1 %	[14]
CZTSSe	Slurries, spin coating (chalcogen-containing precursor)	Se @ 480°C	11.2 %	[15]
CZTSe	Nanoparticle inks (chalcogen-containing precursor)	Se @ 500°C	7.1 %	[9]
CZTS	Spin-coating (chalcogen-containing precursor)	S @ 530°C	n/a	[10]
CZTSSe	Spray pyrolysis (chalcogen-containing precursor)	Se @ 470°C	10 %	[4]
	Physical			
CZTS	Sputtering (Ag- Zn/Cu/Sn)	S @ 570°C	n/a	[16]
CZTSe	Thermal evaporation (Ag- Zn/Cu/Sn)	S @ 570°C	4.4 %	[17]
CZTSe	Sputtering (Ag-Sn/Cu/Zn/Sn/Cu)	Se@ 550°C		[18]

and to enhance grain growth [4, 9, 10]. However, it was experimentally proven that a high concentration of Ag^{+} in CZTS(e) could result in the formation of a weakly n type absorber [11], deteriorating the *p n* junction quality. Consequently, a small concentration is required in order to achieve a good absorber and *p n* junction quality. As sum marized in Table 1, there are several reports on Ag incorporation into the kesterite lattice via a wet chemical route, but only very few using vacuum deposition.

In earlier studies [4, 10], it was demonstrated that the enhancement in grain growth for Ag containing CZTSe (CAZTSe) is due to the liquid assisted grain growth mechanism in connection with the low melting point (217°C) of the eutectic Cu Ag Sn alloy. However, in practice, it remains challenging to form a Cu Ag Sn alloy in a chalcogen con taining precursor prepared from the wet chemical route. Moreover, the formation pathways of the CAZTSe or CAZTS phase via Cu Ag Sn al loys also depends on the precursor configuration and selenization / sulfurization conditions [12, 13]. It is often assumed that for metallic precursors, the kesterite phase is formed via a reaction between bin aries, while for chalcogen containing precursors the reaction proceeds via ternary compounds (Cu Zn Se/S) [13]. In this consideration, there is a narrow window for the reaction pathway to proceed via the for mation of the Cu Ag Sn alloy during annealing of the Ag containing precursor. In addition, the impact of Ag incorporation at the back of precursors on the phase and morphology transition during selenization is not yet investigated. To shed light on this aspect, we performed a temperature dependent analysis of the annealing process of Ag con taining metallic precursors under Se and Sn Se atmosphere with the motivation to elucidate the origin of the large grains observed in CAZTSe absorbers. To evaluate the phase formation during annealing of the co evaporated metallic Ag containing precursors, our standard se lenization protocol was interrupted at different points in the tempera ture profile (see Fig. 1) and the obtained films were investigated using X ray diffractometry (XRD), Raman spectroscopy, and scanning elec tron microscopy (SEM). We further investigated the impact of Ag con centration in the metallic precursors on absorber growth, elemental distribution in the CAZTSe absorber, and the resulting final device performance.

2. Materials and methods

2.1. Film growth and device fabrication

CZTSe and CAZTSe absorbers were synthesized via high tempera ture selenization of co evaporated metallic precursors. The metallic precursors were prepared via a co evaporation of Cu, Zn, and Sn (with 6N purity from ChemPur, Karlsruhe, Germany) onto Mo coated (550 nm) soda lime glass (Mo/SLG) substrates at a temperature of ~100°C using a custom built molecular beam epitaxy system equipped with Knudsen type effusion cells. Precursors were prepared using a deposi tion rate of 1.35 nm/min for Cu, 1.25 nm/min for Zn, and 2.15 nm/min for Sn, respectively, aiming at a precursor with an average bulk
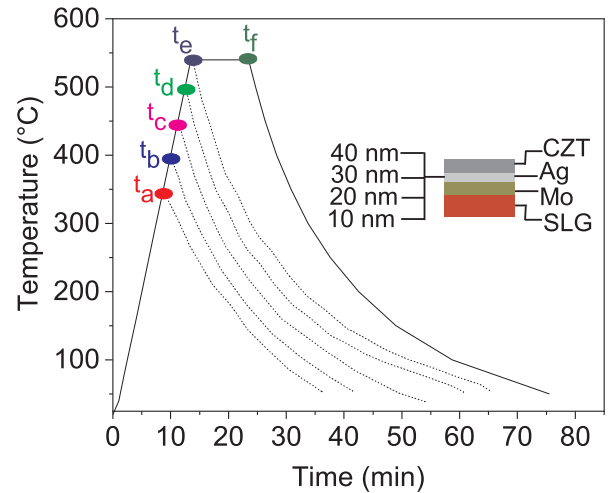

Fig. 1. Temperature profile during selenization of precursor layers with dif ferent interruption temperatures: $t_a = 350$°C, $t_b = 400$°C, $t_c = 450$°C, $t_d = 500$°C, $t_e = 540$°C, and $t_f = 540$°C (10 min). Insert: Layer structure of the device.

elemental composition of [Cu] / ([Zn] + [Sn]) ~ 0.71 and [Zn] / [Sn] ~ 1.01. Prior to deposition, all deposition rates were calibrated sepa rately using a quartz crystal monitor. For CAZTSe absorbers, the Ag layers were thermally evaporated onto Mo coated glass substrates using a belljar thermal evaporation unit (Vactec COAT320) prior to precursor growth. For the Ag film deposition step, the system was evacuated to a pressure of around 10^{-4} Pa. The final concentration of Ag in the ab sorber was varied by changing the thickness of the Ag layer ranging from 10 nm to 40 nm at the bottom of the CZT precursor (see inset graphic in Fig. 1). Prior to selenization, the metallic precursors were alloyed in a N_2 atmosphere at a temperature of 300°C for 15 min. To obtain CZTSe / CAZTSe absorber layers, the alloyed precursors were then annealed in a selenium + tin selenide + N_2 atmosphere utilizing a semi sealed graphite box containing 180 mg of Se and 6 cm (length) of Sn wire placed in a custom built rapid thermal annealing tube furnace. Prior to annealing, the furnace was evacuated to a base pressure of 10^{-4} Pa and then purged with N_2 up to a background pressure of 250 hPa. The furnace was heated to a temperature of 540°C with a ramp rate of 40°C/min, held there for 10 min, and cooled down to room tem perature. The heating process was conducted utilizing a PID controller with previously optimized parameters to avoid any significant tem perature overshoot. Furthermore, the temperature was measured by a thermocouple directly below the sample and connected to the graphite box to ensure correct temperature values. The 10 min period started as soon as the temperature reached 540°C. In order to investigate the phase and morphology transitions during annealing of the metallic and Ag containing metallic precursors, the selenization process was inter rupted at different points in the temperature profile used, as shown in

Fig. 1. The CZTSe and CAZTSe cells were finalized by depositing 50 nm CdS via chemical bath deposition, followed by sputtering 50 nm of intrinsic zinc oxide (*i* ZnO) and 400 nm of ZnO:Al transparent con ducting oxide as a front electrode. Finally, the total active area of 0.16 cm^2 was defined by mechanical scribing.

2.2. Characterization

XRD analysis was carried out using a diffractometer (Bruker D8 Discover) with Cu Kα radiation (λ = 1.54184 Å) operated at 40 kV and 40 mA in a Bragg Brentano geometry at a scan rate of 0.01°/s. To further confirm the material phases in the absorber, Raman spectra were measured between 160 cm^{-1} and 300 cm^{-1} using a Raman spectrometer (Renishaw 1000) equipped with an argon ion laser (Modu Laser, Aries 163, 514.5 nm) and a 50 × objective, resulting in the laser being focused to a diameter of around 1 2 μm. The maximum laser power at the measuring spot was set to 200 μW for all measure ments. To investigate the depth dependent phase distribution across the devices, CZTSe and CAZTSe devices were mechanically polished using a dimple grinder (Gatan Inc. model 656) as proposed in Ref. [19]. The grinder wheel and sample stage were rotating at a normal angle with a velocity of around 4 rpm. A 0.05 μm alumina slurry (ATM GmbH) was used as the polishing suspension.

The absorber morphology was analyzed by SEM (Carl Zeiss SUPRA 55VP, 2 kV acceleration voltage). The depth dependent composition profile was measured using time of flight secondary ion mass spectro metry (ToF SIMS). The corresponding spectrometer (TOF.SIMS5, ION TOF GmbH) was equipped with a Bi cluster primary ion source and a reflectron type time of flight analyzer. The base pressure was < 1×10^{-6} Pa. For high mass resolution, the Bi source was operated in "high current bunched" mode providing short Bi$^+$ primary ion pulses at 25 keV energy, a target current of 1.2 pA, and a lateral resolution of approx. 4 μm. The short pulse length of 0.9 ns allowed for high mass resolution. For depth profiling, a dual beam analysis was performed in interlaced mode: The primary ion source was scanned across an area of 200×200 μm^2 and a sputter gun (operated with O$_2^+$ ions, 2 keV, scanned over a concentric field of 450×450 μm^2, target current 450 nA) was applied to erode the sample. Thereby, the sputter ion dose density was >70000 times higher than the Bi ion dose density. Depth profiles in Fig. 7 (a) (f) are plotted as secondary ion intensities (Σ ^{64}Zn, ^{66}Zn, ^{68}Zn; Σ ^{118}Sn, ^{120}Sn; Σ ^{63}Cu, ^{65}Cu; Σ ^{76}Se, ^{77}Se, ^{78}Se; Σ ^{92}Mo, ^{95}Mo, ^{96}Mo, ^{98}Mo; and Σ ^{107}Ag, ^{109}Ag) normalized to their maximum plotted over sputter ion fluence to obtain an arbitrary depth scale. Note that this scale is usually not linear due to the difference in the sputter yields of different layers.

Current density voltage (*J V*) characteristics were measured using a sourcemeter (Keithley 2400) and illumination via a solar simulator (WACOM single Xe lamp, class AAA) at an intensity of 100 mW/cm^2. The series resistance (R_s) was evaluated by a linear fit to the slope of the *J V* curve around $j_{sc} = 0$ under illumination. Other diode parameters, such as the dark saturation current density (J_o) and diode ideality factor (*n*), were extracted from the dark *J V* data as described in [20, 21]. Temperature dependent current density voltage (*J V T*) measurements were performed in a cryostat (KONTI IT Cryostats, CryoVac) between *T* = 150 K and 300 K in 10 K intervals. External quantum efficiency (EQE) was measured using a system (Bentham PVE300) equipped with both quartz halogen and xenon lamps and calibrated using certified Si and Ge reference detectors.

3. Results and discussion

We first investigated the impact of Ag incorporation on absorber growth by characterizing the structural and morphological properties of CZTSe and CAZTSe films. The XRD patterns for CZTSe and CAZTSe prepared from CZT precursors with different Ag thickness at the back contact are shown in Fig. 2(a). The XRD patterns of both absorber types

agreed with that of the tetragonal CZTSe phase (PDF No. 00 052 0868). However, the XRD peak position (112) shifts towards lower angles with increasing Ag thickness at the bottom of the CZT precursor, as apparent in Fig. 2(b). This strongly indicates that Ag atoms are incorporated in the CZTSe lattice, thus, changing the lattice parameter. Moreover, an increase in peak splitting for the XRD peaks (204)/(220) and (312)/ (116) was observed. This observation is in good agreement with pre vious reports [9, 18]. Using Vegard's law, we estimate the average ratio of [Ag] / ([Ag] + [Cu]) in the films (see Table 2). For the calculation of [Ag] / ([Ag] + [Cu]) ratio, the (112) C(A)ZTSe peak was corrected with respect to the (110) Mo peak and its maximum peak position was ex tracted via a Gaussian fit. As expected, this ratio increases linearly with increasing Ag thickness. Moreover, the calculated lattice constant *a* for C(A)ZTSe increases linearly with rising [Ag] / ([Ag] + [Cu]) ratio, while the lattice constant *c* remains comparable (see Fig 2(c)). This indicates a decreasing *c/a* ratio (see Fig. 2 (d)), resulting in the se paration of the XRD peaks (220)/(204), (312)/(116), and (400)/(008) into individually resolved peaks [18]. Based on these findings, we conclude that Ag is incorporated in the CZTSe lattice, resulting in an increase in the lattice spacing. These findings are in good agreement with previous reports [4, 9, 10, 18].

Fig. 3 shows the Raman spectra of the various C(A)ZTSe absorbers, measured with an excitation wavelength of 514.5 nm. They consist of CZTSe modes detected at 171 cm−1, 195 cm−1, and 233/245 cm−1, respectively. No significant impact of Ag incorporation on the shape of the spectra was found, especially no evidence for deterioration of crystal quality.

Having described the influence of Ag content on the crystal lattice of the C(A)ZTSe absorber, we now look at its impact on the morphology of the absorber. Fig. 4 depicts top view and cross sectional SEM images of C(A)ZTSe absorbers with various Ag concentrations. As can be seen both absorber types are associated with a 1200 nm thick layer of MoSe$_2$ at the back interface. This indicates that a Ag layer cannot efficiently prevent Se diffusion into the Mo back contact. However, the grain size in the absorber layer increases considerably with increasing Ag thick ness at the bottom of the CZT precursor. Based on the [Ag] / ([Ag] + [Cu]) ratios estimated using XRD data (see Table 2), this clearly confirms that a moderate Ag incorporation in the CZTSe ab sorber significantly improves the formation of large grains. For the related copper indium gallium disulfide/diselenide (Cu(In,Ga)(S,Se)$_2$) material, it is well established that a high quality absorber can be ob tained based on a liquid assisted grain growth mechanism from Cu Se and Na Se liquid which promotes elemental diffusion during growth, thus resulting in larger grains and improved crystallinity [22]. A similar concept might be applicable to CZTSe absorbers as well. However, in the case of Ag incorporation, it is often assumed that a Cu Ag Sn alloy contributes to the enhanced liquid assisted grain growth, resulting in large grains and a better crystallinity of the CZTSe absorber [8 10].

As a proof of concept, we investigated the phase and morphology transitions during annealing of the CZT precursor with and without Ag layer at the bottom. To elucidate this, we interrupted our selenization process at different points in the temperature profile (as illustrated in Fig. 1) and analyzed the obtained films using XRD, micro Raman spectroscopy, and SEM. We first investigated the material phases pre sent in the CZT precursor. As illustrated in Fig. 5(a) (black line), the precursor contains the alloys Cu$_{10}$Sn$_3$ (PDF No. 03 065 3632), Cu$_3$Sn (PDF No. 00 001 1240), Cu$_6$Sn$_5$ (PDF No. 00 047 1575), Cu$_5$Zn$_8$ (PDF No. 00 025 1228), CuZn (PDF No. 00 002 1231), and Cu$_{40.5}$Sn$_{11}$ (PDF No. 01 071 0121), together with elemental Sn (PDF No. 03 065 0296). The absence of alloys after annealing the film at 350°C (t$_a$) confirms that the process starts by decomposition of alloys and formation of selenides (see Fig. 5(a)). The Raman spectra showed the co existence of Cu$_2$SnSe$_3$ (Raman mode at 178 cm^{-1}) together with CZTSe (Raman modes at 233 cm^{-1} and 245 cm^{-1}), revealing an early formation of the CZTSe phase. Concerning film morphology, we observed a rough sur face and fine grains across the absorber. Increasing the selenization
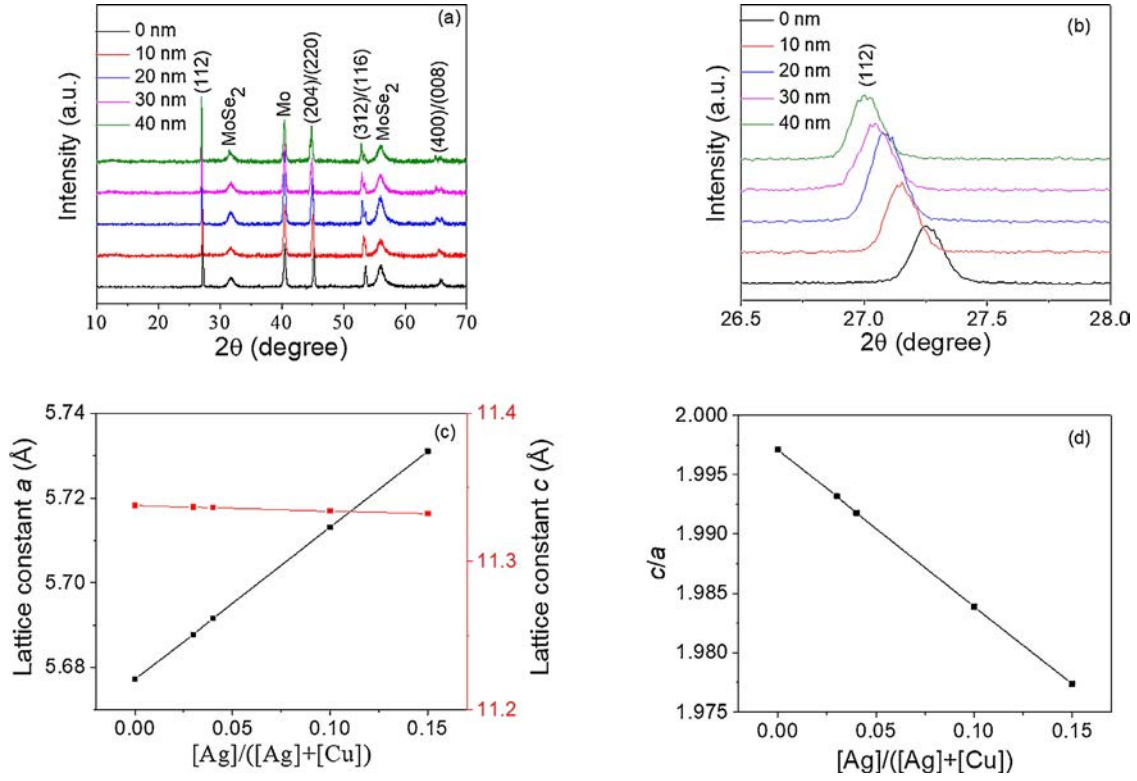
Fig. 2. (a) XRD scans, (b) detailed view of the (112) XRD peak, (c) lattice constants a and c, and (d) the ratio of the C(A)ZTSe absorbers prepared from CZT precursors with different Ag thickness at the back contact.

Table 2

(112) XRD peak positions and resulting [Ag] / ([Ag] + [Cu]) ratios for C(A) ZTSe absorbers prepared from CZT precursors with different Ag thickness at the bottom.

Ag thickness (nm)	0	10	20	30	40
(112) XRD peak position (°)	27.26	27.12	27.09	27.04	26.99
[Ag] / ([Ag] + [Cu])	0	0.03	0.05	0.10	0.15
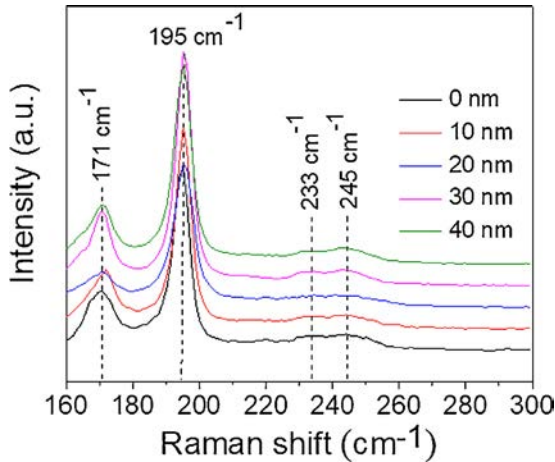
Fig. 3. Raman spectra of the C(A)ZTSe absorbers prepared from CZT precursors with different Ag thickness at the back contact.

temperature to point t_b led to the formation of $SnSe_2$ and $CuSe_2$ (see Fig. 5(a)), indicating that the process is under Se overpressure. No significant change in sample morphology was observed. Moreover, when the temperature reaches point t_c, Raman spectra indicated a dominance of the CZTSe and the $SnSe_2$ phases while the $SnSe_2$ and

$CuSe_2$ phases together with CZTSe were visible in XRD (see Figs. 5(a and c)). The results we obtained at this temperature regime differ somewhat from those reported by Giraldo *et al.* during the selenization of sputtered stacked precursors [23], where it was demonstrated that above 400°C, the $CuSe_2$ phase is reduced to the Cu_2Se phase. However, it was proposed [23, 24] that the formation of the $CuSe_2$ phase depends on the Se partial pressure in the graphite box. The morphology of the sample in this temperature regime was characterized by fine grains (see Fig. 6 (c1)). At the surface of the sample annealed at 500°C (t_d) and 540°C (t_e), only the CZTSe phase was present. Based on these results it would be feasible that the rate of morphology transition is relatively low, indicating grain growth and redistribution occur at 540°C and during holding time.

To investigate the phase and morphology transitions during annealing of Ag CZT, 20 nm Ag was deposited at the bottom of the CZT layer. Fig. 5(b) shows XRD patterns of the Ag CZT precursors annealed at different temperatures. The Ag CZT precursor comprised alloys of $Cu_{10}Sn_3$, Ag_4Sn (PDF No. 00 029 1151), Cu_5Zn_8, Cu_6Sn_5, CuZn, and $Cu_{40.5}Sn_{11}$, together with elemental Sn. No alloy related to Cu Ag Sn was detected. After the selenization of the Ag CZT precursor at 350°C (Fig. 5(b)), all alloys decomposed or converted to selenide compounds as discussed for the CZT precursors. At this temperature, special attention was paid to the CZTSe related XRD peaks. A major peak was observed at $2\theta \approx 27.16°$ with a shoulder at $2\theta \approx 27.30°$, as well as the XRD peak at 45.35° that exhibited a double structure at $2\theta \approx 44.9°$ and 45.35°. This implies that more than one phase co exists with CZTSe. The XRD peaks at $2\theta \approx 27.30°$ and 45.35° correspond to $AgSnSe_2$ (PDF No. 00 033 1194) while that at 44.9° is related to the Ag_2Se phase (PDF No. 00 024 1041). In order to get further information about the selenide compounds in these films, micro Raman spectroscopy was performed.

As illustrated in Fig. 5(d), we observed broad peaks at around 178 cm^{-1} and 245 cm^{-1}, respectively, with the tail extending up to 260 cm^{-1}. This strongly suggests that the surface of the analyzed sample contains a mixture of CAZTSe and Cu_2SnSe_3. Concerning the
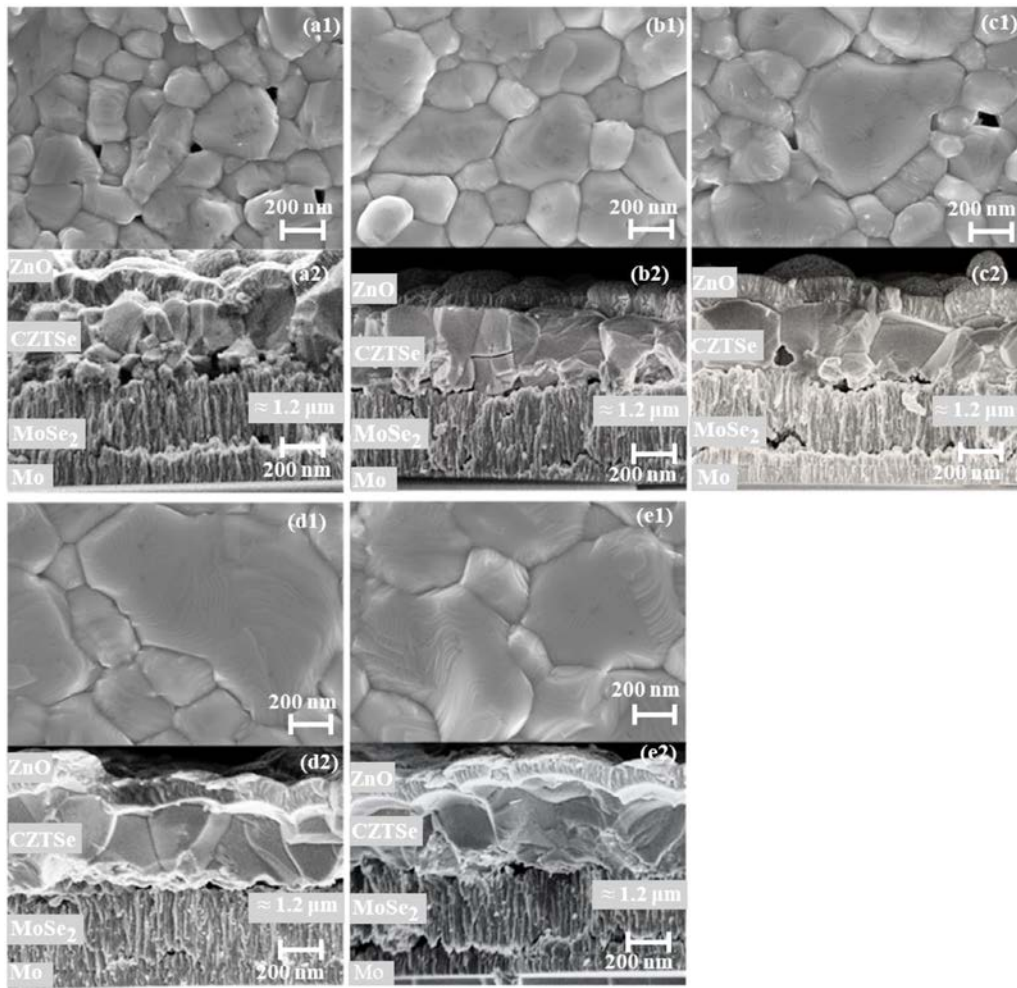
Fig. 4. Top-view (top) and cross-sectional (bottom) SEM images of C(A)ZTSe absorbers prepared from (a) 0 nm, (b) 10 nm, (c) 20 nm, (d) 30 nm, and (e) 40 nm of Ag thickness at the bottom of the CZT precursors.

morphology of this sample, we observed a mixture of large and small grains with a rough surface (see Fig. 6 (a2)). Interestingly, when the selenization temperature reaches point t_b, the major XRD peak at $2\theta \approx 27.16°$ shifted to the lower 2θ value ($2\theta \approx 26.60°$) and a clear se paration of the XRD peaks at $2\theta \approx 27.30°$ and $45.35°$ was found (see Fig. 5 (b), blue line). We observed extinction of the Ag_2Se phase ($2\theta \approx 44.90°$) and evolution of $2\theta \approx 44.50°$ which can be assigned to the Cu_2Se phase (PDF No. 03 065 2982) (see Fig. 5 (c)). The confirmation of the XRD peak at $2\theta \approx 26.60°$ and the extinction of the Ag_2Se phase strongly indicate the formation of the Ag rich CAZTSe phase. To further address this aspect, a pure Ag kesterite ($Ag_2ZnSnSe_4$ (AZTSe)) film was prepared and analyzed using XRD. Fig. 7 shows the XRD pattern of the AZTSe film. The pattern agreed with that of the tetragonal AZTSe phase with a major (112) peak at $26.10°$ [25]. With these observations, we conclude that the XRD peak at $2\theta \approx 26.60°$ could be assigned to the Ag rich CAZTSe films. When the selenization temperature reaches point t_c, the intensity of the XRD peak corresponding to the $AgSnSe_2$ phase significantly reduced and the main XRD peak shifted back to $2\theta \approx 27.08°$. We observed a re evolution of the Ag_2Se phase at $2\theta \approx 44.90°$ and a significant decrease in the intensity of the peak at $2\theta \approx 45.35°$ ($AgSnSe_2$ phase, see Fig. 5 (b)). This implies that most of the AZTSe and $AgSnSe_2$ phases were decomposed and converted to the Ag_2Se and CAZTSe phase. The Raman spectra reveal that the surface of this sample contains the kesterite (Raman modes at $168\ cm^{-1}$, $195\ cm^{-1}$, and $233/245\ cm^{-1}$) and the $SnSe_2$ ($184\ cm^{-1}$) phases (see Fig. 5 (d)). With respect to morphology, we observed large grains across the whole layer,

confirming that the formation of the CAZTSe phase is associated with grain growth. When temperature increases to point t_d, CAZTSe, $SnSe_2$, Ag_2Se, and $CuSe_2$ remain as the main material phases (see Fig. 5 (b)) in the layer. The surface of the film consisted of the CAZTSe and the $SnSe_2$ phase (see Fig. 5 (d)). Looking at the morphology, large grains across the layer can be seen. Moreover, there was no indication of $MoSe_2$ formation at this temperature. Increasing selenization temperature to point t_e, the surface of the film contained only the CAZTSe phase. However, the XRD pattern in Fig. 5 (b) still indicated the dominance of $SnSe_2$ over the CAZTSe phase. Only when the sample is annealed for 10 min, the XRD pattern finally showed the dominance of the CAZTSe phase. However, the XRD peak at $2\theta \approx 45.10°$ with a shoulder at $44.80°$ still indicated the existence of a secondary phase (Ag_2Se).

Comparing the phase and morphology transitions of the CZT and Ag CZT precursor, we can conclude that in both cases the formation of the CZTSe and Cu_2SnSe_3 phases start at low temperature. Ag in corporation in the precursor changes the rate of morphology transition (see Fig. 6). However, the confirmation of the Ag_2Se phase (see Fig. 5 (b)) in the course of the CAZTSe growth suggests that the Ag Se phase plays a critical role in larger grain formation. Considering the CZTSe sister technology, $Ag_2ZnSnSe_4$ (AZTSe) thin films, Gershon *et al.* sug gested that the formation of the Ag Se phase acts as a fluxing agent and promotes the recrystallization of AZTSe [26]. Based on our own find ings and reports from the literature [23, 26, 27], we, therefore, suggest that the formation of the Ag Se liquid phase speeds up the rate of Ag Sn Se, Cu Ag Sn Se, and CAZTSe phase formation, and
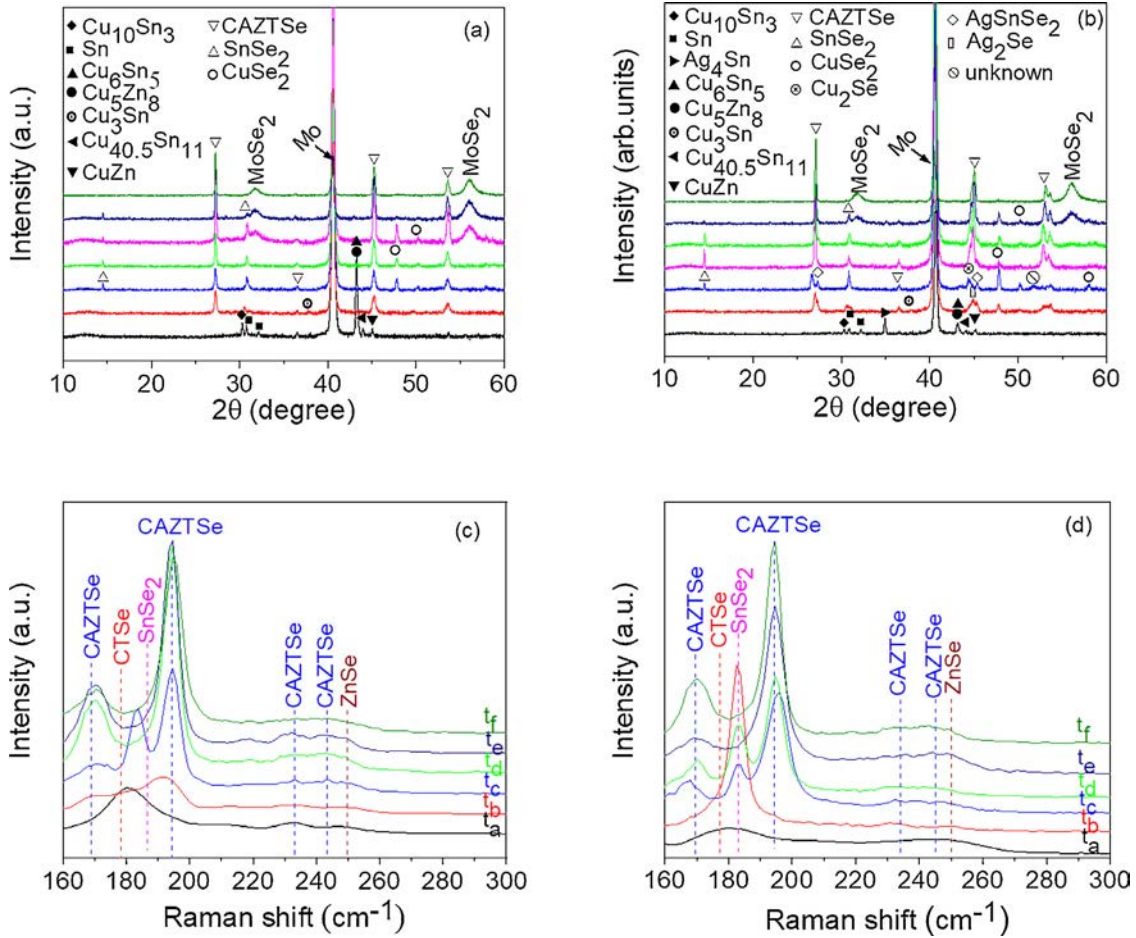
Fig. 5. (a) and (b): XRD patterns of the films prepared from CZT and Ag–CZT precursors, respectively, produced when the annealing process was interrupted at different temperatures. (c) and (d): Corresponding Raman spectra. Labeling according to Fig. 1.

consequently absorber recrystallization.

In order to investigate the Ag distribution across the absorber and the formation of the interface layers, we performed ToF SIMS depth profile measurements on complete devices, focusing on the distribution of Cu, Zn, Sn, Se, Ag, and Mo across the structures. Using the signals of Se and Mo, the position of window layer, absorber, $MoSe_2$, Mo, and SLG were identified (see Fig. 8). As we erode from the surface of all devices, no signals of Cu, Sn, Se, and Ag were detected until we reached a flu ence of around 1.0×10^{18} ions/cm^2. This confirms that we eroded through the window layer to the absorber layer. The distributions of Cu, Zn, Sn, Se, and Ag across the absorber are fairly homogenous. The homogenous distribution of Ag across the absorber reveals that Ag es sentially diffuses uniformly from the back to the surface during sele nization and is incorporated in the CZTSe lattice to form CAZTSe. When erosion reached around 2.7×10^{18} ions/cm^2, the signal of Cu, Sn, and Ag significantly decreased while that of Zn almost vanished. The signal of Se and Mo significantly increased, indicating we reached the $MoSe_2$ layer. The significant increase in Mo and Se signals confirmed that the density of the absorber strongly differs from that of the $MoSe_2$ layer, consequently, the erosion rate varied substantially. We further detected the signal of Cu and Sn for the devices with CZTSe absorber (see Fig. 8 (a)), while Cu, Sn, and Ag signals were present for the case of CAZTSe (see Fig. 8 (b e)). The absence of a Zn signal (it vanished at around 3.40×10^{18} ions/cm^2) strongly suggested that Cu, Sn, and Ag out dif fuse to the $MoSe_2$ layer from the absorber and accumulate at the $MoSe_2$/Mo interface. Dalapati *et al.* made similar observations and re lated them with Mo out diffusion in the absorber during the sulfuriza tion of the sputtered precursors [28]. To further address this aspect,

depth dependent Raman spectra (dimpling Raman spectra) were ac quired on a complete device prepared from a precursor with 40 nm of Ag at the bottom in order to analyze the $MoSe_2$/Mo interface (position L1), $MoSe_2$ layer (position L2), and CZTSe back and surface (positions L3 and L4), see Fig. 9 (a and b). Note that since an excitation wave length of 514.5 nm was used, the probing depth should be low and in the order of 100 nm.

As illustrated in Fig. 9 (c), at the $MoSe_2$/Mo interface (position L1), the spectra exhibited Raman modes at 167 cm^{-1}, 240 cm^{-1}, 285 cm^{-1}, and 350 cm^{-1}, respectively, corresponding to $MoSe_2$. As expected, the Raman modes related to $MoSe_2$ were visible at position L2 and almost vanished at positions L3 and L4 (CAZTSe absorber). Moreover, a Raman mode at 300 cm^{-1} related to CdS was detected at position L3 and L4. We observed a similar trend in other samples (not shown here). This is an artifact due to the redeposition of CdS during mechanically polishing the CAZTSe devices. The presence of Cu, Sn, and Ag at the $MoSe_2$ and $MoSe_2$/Mo interface could be related to the sputtering process leading to the diffusion of those elements during the erosion of layers (mea suring artifacts). Concerning the Ag distribution in the absorber, we plot the intensity of the Ag signal vs. fluence (see Fig. 8 (f)). The depth integrated Ag signals are scaling nearly linearly with the applied nominal Ag layer thicknesses (530, 960, 1370, and 1800 kcts on sam ples with 10, 20, 30, 40 nm Ag, respectively). These findings confirm that Ag atoms are homogeneously incorporated in the absorber. How ever, our observations are somewhat different from those reported in [18]. It was observed that at the surface the concentration of Ag was higher than at the back of the absorber, consequently, a front bandgap gradient was demonstrated. This discrepancy could be related to the
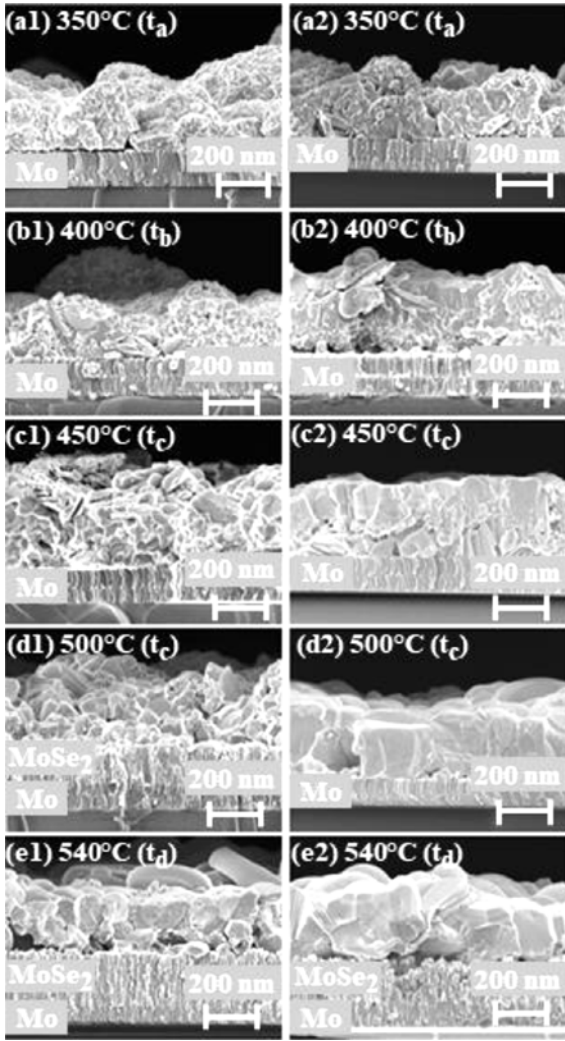
Fig. 6. Cross-sectional SEM images of the films obtained when the annealing process was interrupted at different points in the temperature profile of the selenization process. Left column (a1–e1): films prepared from CZT precursors. Right column (a2–e2): films prepared from Ag–CZT precursor.
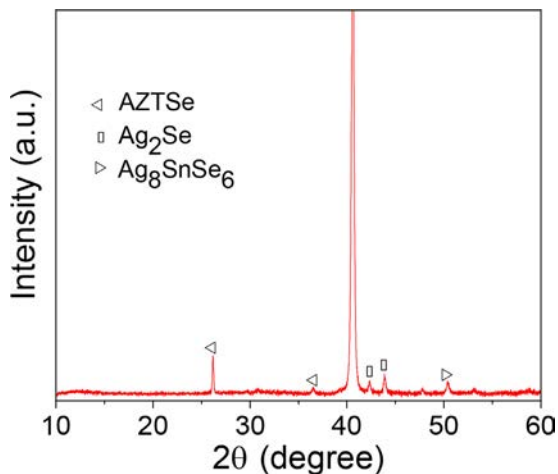

Fig. 7. The XRD pattern of an AZTSe film prepared from Ag–Zn–Sn precursor.

precursor configuration. The stacked precursor configuration might provide a depth gradient composition that should invoke different reaction pathways, resulting in the Ag front gradient [18, 21]. Regarding

Na distribution in the C(A)ZTSe absorber, we observe a suppression of Na diffusion from the SLG to the absorber layer. However, no clear trend for various Ag layer thicknesses at the back of CZT was observed (see Table 3).

Having described the impact of Ag incorporation on the structural properties and elemental distribution of the CAZTSe absorber, we now look at its influence on device performance. To this end, the dark and illuminated J V characteristics of the various structures were measured and evaluated. In Fig. 10 (a), the J V curves of the champion solar cells on the five samples with different Ag thickness at the bottom of the precursor are shown, corresponding to the solar cell parameters in Table 3. As displayed in Fig. 10 (a) and Table 3, the J V curves and solar cell parameters are strongly influenced by the thickness of Ag at the bottom of the CZT precursor. The reference sample without Ag at the bottom of the CZT layer yielded a maximum conversion efficiency η of 6.9 % (6.2 % on average, four cells), with a V_{OC} and FF of 390 mV (380 mV on average) and 50 % (48 % on average), respectively. For the case of 10 nm of Ag deposited at the bottom of the CZT precursor, η increased up to 7.6 % (6.9 % on average, four cells). This improvement mainly results from a significant increase in V_{OC} (from 390 mV to 428 mV). Increasing the Ag thickness beyond 10 nm leads to a poorer device performance with η dropping from 7.6 % (10 nm) to 3.0 % (40 nm) (2.6 % on average), see Table 3. A similar trend can be seen in V_{OC}, FF, and j_{SC}. Considering the R_S of the devices (increasing from around 3.1 Ωcm^2 (3.5 Ωcm^2, on average) (10 nm) to 10.2 Ωcm^2 (9.0 Ωcm^2 on average) (40 nm)), it is not surprising to observe a similar trend (see Table 3). These findings are in agreement with wet chemically processed devices reported in the literature [4, 8, 9] but not expected based on absorber morphology (Fig. 4), since the latter improves with a further increase in Ag thickness at the bottom of the CZT precursor. Ag incorporation in the CZTSe absorber is expected to induce Ag related defects such as Ag_{Zn} antisite defects. From theoretical and experimental results these defects could be donor like and result in compensation effects in the p type absorber [18, 26, 29, 30]. As a result of this, the resistance of CAZTSe would increase which could influence the device performance and particularly have an impact on the series resistance of the solar cells [30].

It is well known that Ag incorporation in CZTSe tunes the bandgap of the resulting CAZTSe material, leading to changes in V_{OC} and j_{SC} of the solar cells. Using EQE data, the bandgap of the absorber was esti mated, as illustrated in Fig. 10 (c). Interestingly, the bandgap stayed almost constant at around 1.04 eV for the Ag free reference and 1.09 eV for the devices containing 40 nm Ag. This reveals that the amount of Ag incorporated in the CZTSe lattice was not high enough to significantly change the absorber bandgap, in good agreement with XRD and Raman measurements. Based on these findings, we conclude that the increase in V_{OC} observed from the solar cell with 10 nm of Ag at the bottom of the CZT precursor is at least partly due to other reasons, most likely the improvement of grain growth (see Fig. 4 (b)) and band alignment at CdS/CZTSe interface [14]. However, this could not explain the poor performance of the devices prepared from precursors with Ag thickness beyond 10 nm. The ideality factor (n) for all devices stays above 2 (see Table 3), strongly indicating an unusual recombination mechanism in the devices. Possible candidates for the corresponding recombination mechanisms are tunneling enhanced recombination (in the space charge region), recombination via coupled defects, and donor acceptor pair recombination [31]. To further address this aspect, we performed EQE measurements for all devices. Fig. 10 (b) shows the EQE spectra for solar cells prepared from CZT precursors with different Ag layer thicknesses at the bottom. The general and maximum EQE response decrease with increasing Ag layer thickness, suggesting the presence of Ag related defects. The EQE response for all devices prepared from CAZTSe absorbers decreases in the longer wavelength region compared to devices from CZTSe absorbers. This suggests significant recombina tion losses in the absorber bulk (due to Ag induced defects), although interface defects may also contribute to the general decrease. To further
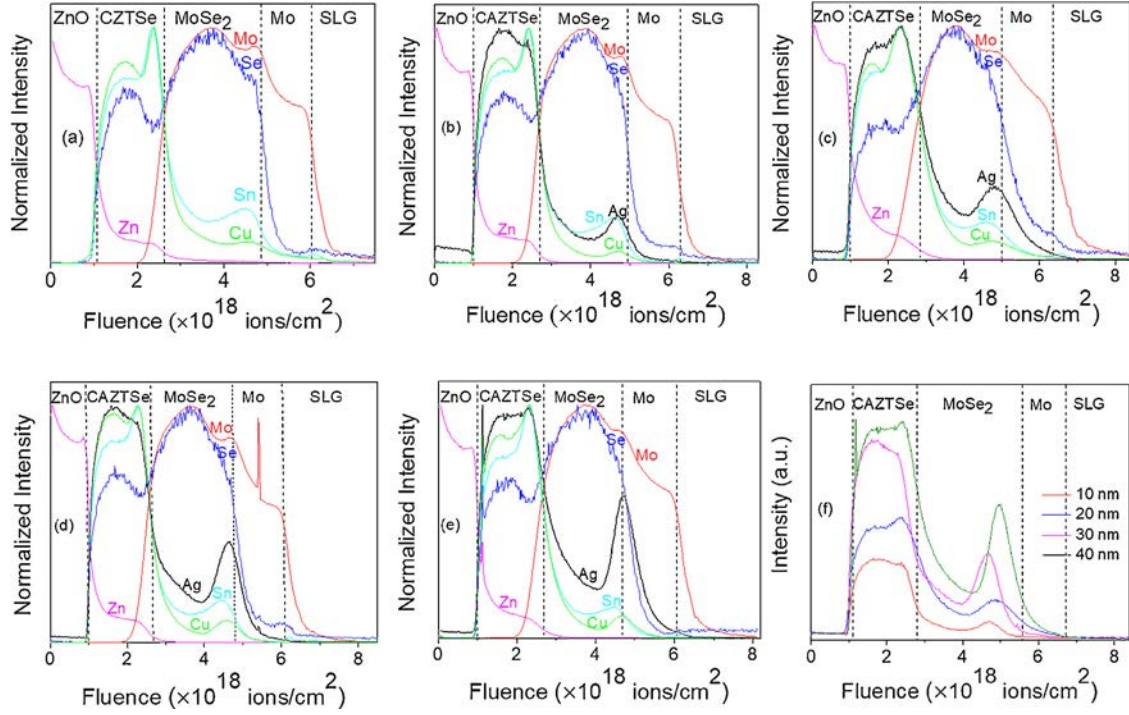
Fig. 8. ToF-SIMS profiles of solar cells with various absorbers. (a) CZTSe absorber prepared from a CZT precursor. (b–e) CAZTSe absorbers prepared from CZT precursors with Ag thickness of 10 nm, 20 nm, 30 nm, and 40 nm at the bottom, respectively. (f) Ag distribution in the absorber and at the MoSe$_2$/Mo interface for precursors with different Ag layer thicknesses.

investigate this, J V T measurements were performed and analyzed as described in the literature [31 33]. The relationship between V_{OC} and temperature is commonly used to determine the activation energy (E_A) of the main recombination mechanism in thin film solar cells. Fig. 10 (d) shows the dependence of V_{OC} on temperature, with an extrapolation to $T = 0$ K yielding the E_A of the main recombination mechanism. The E_A of a device prepared from the CZTSe absorber (0 nm of Ag) was very close to the bandgap extracted from EQE measurements. In contrast, the E_A of the devices prepared from CAZTSe (10 nm to 40 nm of Ag) was lower than the bandgap extracted from EQE (see Fig. 10 (c)). Based on these findings we conclude that while bulk recombination is dominant in devices prepared from CZTSe absorbers, the CdS/CAZTSe interface

Table 3

Relative Na content in C(A)ZTSe absorbers prepared from CZT precursors with 0 nm, 10 nm, 20 nm, 30 nm, and 40 nm of Ag at the bottom of the precursor, respectively.

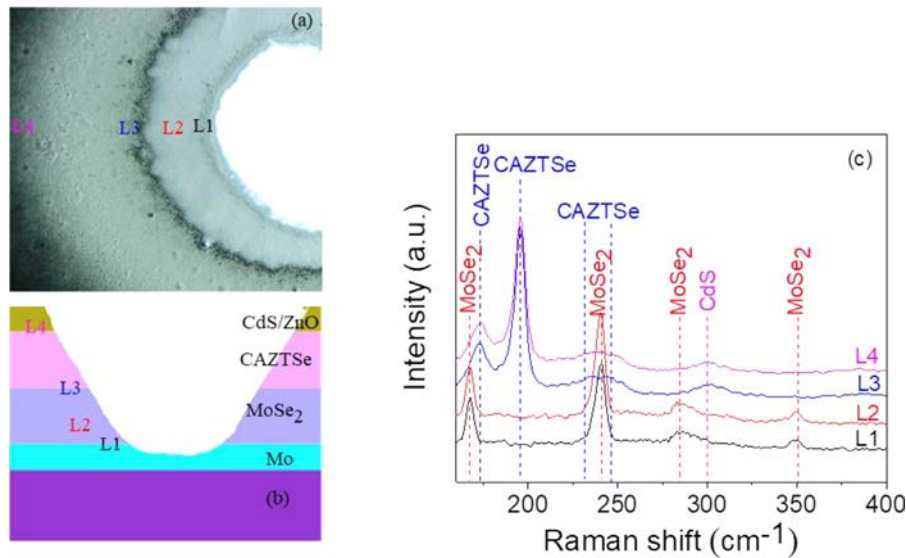| Sample	Relative Na content in absorber layer (%)
0 nm	100
10 nm	19
20 nm	54
30 nm	13
40 nm	31

Fig. 9. (a) Optical microscope image of a dimpled CAZTSe solar cell. (b) Schematic diagram of a dimple depicting Raman measurement regions with respect to different layers (c) Depth-dependent Raman spectra for a CZTSe solar cell prepared from a CZT precursor without Ag.

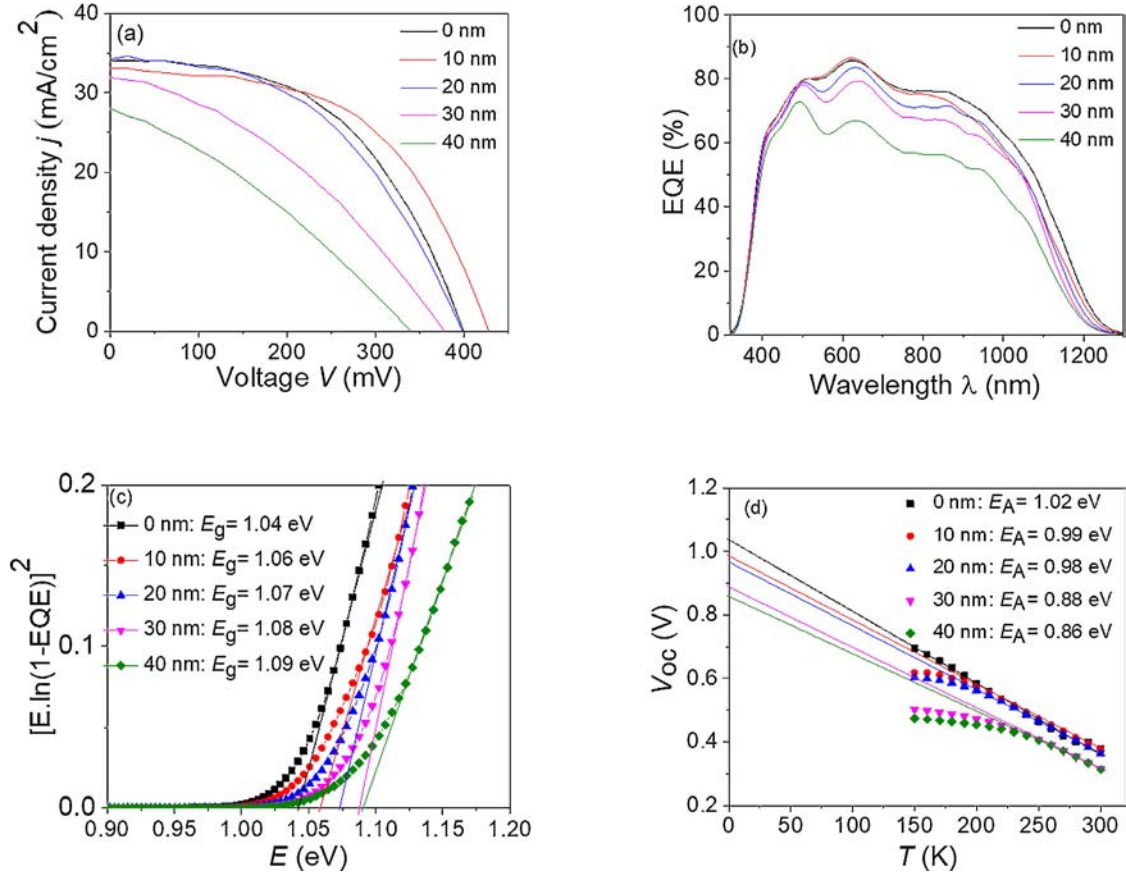| Sample	η (%)	FF (%)	V_{OC} (mV)	J_{SC} (mA/cm^2)	R_S (Ωcm^2)	n	j_O ($\times 10^{-5}$ mA/cm^2)
0 nm	6.9 (6.2 [‡])	50 (48 [‡])	390 (380 [‡])	34 (34 [‡])	3.4 (3.4 [‡])	2.7 (2.7[‡])	3.6 (4.9 [‡])
10 nm	7.6 (6.9 [‡])	54 (51 [‡])	428 (408 [‡])	33 (34 [‡])	3.1 (3.5 [‡])	2.7 (2.4 [‡])	0.6 (0.4 [‡])
20 nm	6.5 (6.2 [‡])	48 (46 [‡])	398 (390 [‡])	34 (34 [‡])	4.0 (4.1 [‡])	2.5 (2.8 [‡])	0.5 (2.6 [‡])
30 nm	4.4 (4.0 [‡])	36 (36 [‡])	378 (353 [‡])	32 (31 [‡])	6.6 (6.4 [‡])	2.5 (2.3 [‡])	0.3 (6.3 [‡])
40 nm	3.0 (2.6 [‡])	32 (31 [‡])	340 (323 [‡])	28 (27 [‡])	10.2 (9 [‡])	2.5 (2.5 [‡])	0.2 (1.7 [‡])

[‡]Average device parameters

Fig. 10. (a) Current density–voltage characteristics, (b) EQE spectra, (c) bandgap estimated by $[E \cdot \ln(1\text{-EQE})]^2$ vs E, and (d) variation of V_{OC} vs. temperature for solar cells prepared from CZT precursors with 0 nm, 10 nm, 20 nm, 30 nm, and 40 nm of Ag at the bottom of the precursor, respectively.
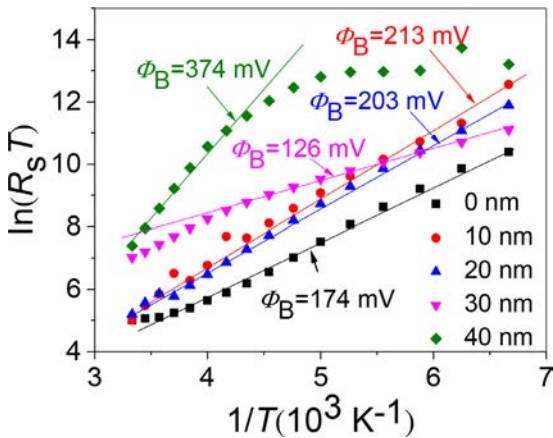

Fig. 11. ln(RST) versus 1/T for C(A)ZTSe devices prepared from CZT precursors with different Ag thickness at the back contact.

contributes more significantly to recombination losses in Ag containing devices. Nevertheless, the presence of Ag also seems to enhance bulk recombination. For instance, inclusions of the Ag$_2$Se phase in the main CAZTSe absorber material may lead to a deterioration of device performance [31]. The Schottky barrier height extracted from an Arrhenius plot of the temperature dependent dark R_S (see Fig. 11) showed no trend with Ag thickness at the back of the precursors. This suggests that the Ag layer at the back of the precursor does not act as an efficient temporary barrier for Se during selenization as proposed in previous reports [17, 30]

4. Conclusions

In summary, we investigated the influence of Ag incorporation at the back interface of vacuum deposited C(A)ZTSe absorbers on their growth properties and resulting solar cell performance. From ToF SIMS measurements we found that after the selenization of the Ag CZT precursors, Ag is essentially uniformly distributed across the absorber. Ag incorporation mainly affects grain formation. Based on temperature

dependent analyses of the reaction pathway during precursor seleni zation using XRD, Raman spectroscopy, and SEM morphology studies, we presented evidence suggesting that the formation of large grains in CAZTSe absorbers is attributed to a Ag Se liquid assisted grain growth mechanism. We observed that with very thin Ag layers (10 nm) at the back contact, efficiency is enhanced from 6.9 % (Ag free reference solar cells) to 7.6 %   mainly due to an increase in the open circuit voltage (from 390 mV to 428 mV), while thicker layers lead to device dete rioration related to both enhanced bulk and interface recombination. We expect that a continuing optimization of both annealing tempera ture and time should enable further improvement of device perfor mance.

Credit author statemen Lwitiko

Lwitiko Pholds Mwakyusa: Conceptualization, methodology, sample and devices fabrication characterization, and writing original draft prepartion. **Lennart Leist**: Sample and device fabrication. **Alexander Welle**: ToF SIMS analysis and discussion. **Monika Rinke:**Raman Measurement and discussion. **Ulrich W. Paetzold, Bryce S. Richards, and Michael Hetterich:**Supervision, methodology, and Writing Reviewing and editing the manuscript.

Declaration of Competing Interest

None.

Acknowledgments

References

[1] Z. Song, J.S. Jang, J.H. Yun, H. Cheong, Y. Yan, Band tail engineering in kesterite Cu2ZnSn(S,Se)4 thin-film solar cells with 11.8% efficiency, J. Phys. Chem. Lett. 9 (2018) 4555–4561, https://doi.org/10.1021/acs.jpclett.8b01433.

[2] V.A. online, fabricated by sputtering a Cu – Zn – Sn – Se quaternary compound target with a selenization, (2019) 9948–9957. doi:10.1039/c9ta00385a.

[3] W. Wang, M.T. Winkler, O. Gunawan, T. Gokmen, T.K. Todorov, Y. Zhu, D.B. Mitzi, Device characteristics of CZTSSe thin-film solar cells with 12.6% efficiency, Adv. Energy Mater. 4 (2014) 1301465-n/a, , https://doi.org/10.1002/aenm.201301465.

[4] W.C. Huang, S.Y. Wei, C.H. Cai, W.H. Ho, C.H. Lai, The role of Ag in aqueous solution processed (Ag,Cu)2ZnSn(S,Se)4kesterite solar cells: antisite defect elim ination and importance of Na passivation, J. Mater. Chem. A. 6 (2018) 15170–15181, https://doi.org/10.1039/c8ta02950d.

[5] T. Gershon, D. Bishop, P. Antunez, S. Singh, K.W. Brew, Y.S. Lee, O. Gunawan, T. Gokmen, T. Todorov, R. Haight, Unconventional kesterites: the quest to reduce band tailing in CZTSSe, Curr. Opin. Green Sustain. Chem. 4 (2017) 29–36, https://doi.org/10.1016/j.cogsc.2017.01.003.

[6] M. Lang, C. Zimmermann, C. Krämmer, T. Renz, C. Huber, H. Kalt, M. Hetterich, Luminescence properties of Cu 2 ZnSn (S, Se) 4 solar cell absorbers : State filling versus screening of electrostatic potential fluctuations, 155202 (2017) 1–9. doi:10. 1103/PhysRevB.95.155202.

[7] A. Phys, M. Lang, T. Renz, A. Opolka, C. Zimmermann, C. Krämmer, M. Neuwirth, H. Kalt, M. Hetterich, Impact of the degree of Cu – Zn order in Cu2ZnSn (S, Se) 4 solar cell absorbers on defect states and band tails, 033901 (2018) 1–6. doi:10. 1063/1.5036622.

[8] Y. Qi, Q. Tian, Y. Meng, D. Kou, Z. Zhou, W. Zhou, S. Wu, El (Cu 1 emental pre cursor solution processed   , (2017) 1–8. doi:10.1021/acsami.7b03944.

[9] C.J. Hages, M.J. Koeper, R. Agrawal, Optoelectronic and material properties of

[10] J. Kumar, S. Ingole, Structural and optical properties of (AgxCu1-x)2ZnSnS4 thin films synthesised via solution route, J. Alloys Compd. 727 (2017) 1089–1094, https://doi.org/10.1016/j.jallcom.2017.08.222.

[11] Z. Absorber, T. Gershon, K. Sardashti, O. Gunawan, R. Mankad, S. Singh, Y.S. Lee, J. A. Ott, A. Kummel, R. Haight, Photovoltaic device with over 5 % efficiency based on, (2016). doi:10.1002/aenm.201601182.

[12] D.H. Son, D.H. Kim, S.N. Park, K.J. Yang, D. Nam, H. Cheong, J.K. Kang, Growth and device characteristics of CZTSSe thin-film solar cells with 8.03% efficiency, Chem. Mater. 27 (2015) 5180–5188, https://doi.org/10.1021/acs.chemmater. 5b01181.

[13] A. Hernandez Martinez, M. Placidi, L. Arques, S. Giraldo, Y. Sánchez, V. Izquierdo-Roca, P. Pistor, M. Valentini, C. Malerba, E. Saucedo, Insights into the formation pathways of Cu 2 ZnSnSe 4 using rapid thermal processes, ACS Appl. Energy Mater. (2018), https://doi.org/10.1021/acsaem.8b00089 acsaem.8b00089.

[14] T.H. Nguyen, T. Kawaguchi, J. Chantana, T. Minemoto, T. Harada, S. Nakanishi, S. Ikeda, Structural and solar cell properties of a Ag-containing Cu2ZnSnS4thin film derived from spray pyrolysis, ACS Appl. Mater. Interfaces. 10 (2018) 5455–5463, https://doi.org/10.1021/acsami.7b14929.

[15] Y.F. Qi, D.X. Kou, W.H. Zhou, Z.J. Zhou, Q.W. Tian, Y.N. Meng, X.S. Liu, Z.L. Du, S.X. Wu, Engineering of interface band bending and defects elimination via a Ag-graded active layer for efficient (Cu,Ag)2ZnSn(S,Se)4solar cells, Energy Environ. Sci. 10 (2017) 2401–2410, https://doi.org/10.1039/c7ee01405h.

[16] W. Li, X. Liu, H. Cui, S. Huang, X. Hao, The role of Ag in (Ag,Cu)2ZnSnS4thin film for solar cell application, J. Alloys Compd. 625 (2015) 277–283, https://doi.org/ 10.1016/j.jallcom.2014.11.136.

[17] H.T. Cui, X.L. Liu, F.Y. Liu, X.J. Hao, N. Song, C. Yan, Boosting Cu2ZnSnSnS4 solar cells efficiency by a thin Ag intermediate layer between absorber and back contact, Appl. Phys. Lett. 104 (2014) 041115, , https://doi.org/10.1063/1.4863951.

[18] D. Wang, J. Wu, X. Liu, L. Wu, J. Ao, W. Liu, Y. Sun, Y. Zhang, J. Wu, X. Liu, L. Wu, J. Ao, W. Liu, Y. Sun, Y. Zhang, PT US CR (2019), https://doi.org/10.1016/j. jechem.2019.03.026.

[19] D.-K. Hwang, B.-S. Ko, D.-H. Jeon, J.-K. Kang, S.-J. Sung, K.-J. Yang, D. Nam, S. Cho, H. Cheong, D.-H. Kim, Single-step sulfo-selenization method for achieving low open circuit voltage deficit with band gap front-graded Cu2ZnSn(S,Se)4 thin films, Sol. Energy Mater. Sol. Cells. 161 (2017) 162–169, https://doi.org/10.1016/ j.solmat.2016.11.034 doi:https://doi.org/.

[20] M. Neuwirth, E. Seydel, J. Seeger, A. Welle, H. Kalt, M. Hetterich, Band-gap tuning of Cu2ZnSn(S,Se)4 solar cell absorbers via defined incorporation of sulphur based on a post-sulphurization process, Sol. Energy Mater. Sol. Cells. 182 (2018) 158–165, https://doi.org/10.1016/j.solmat.2018.03.033 doi:https://doi.org/.

[21] L.P. Mwakyusa, M. Neuwirth, W. Kogler, T. Schnabel, E. Ahlswede, U.W. Paetzold, B.S. Richards, M. Hetterich, CZTSe solar cells prepared by co- evaporation of multilayer Cu – Sn / Cu, Zn, Sn, Se / ZnSe / Cu, Zn, Sn, Se stacks, (2019).

[22] C. Gao, T. Schnabel, T. Abzieher, E. Ahlswede, M. Powalla, M. Hetterich, Preparation of Cu2ZnSnSe4solar cells by low-temperature co-evaporation and fol lowing selenization, Appl. Phys. Lett. (2016) 108, https://doi.org/10.1063/1. 4939445.

[23] S. Giraldo, E. Saucedo, M. Neuschitzer, F. Oliva, M. Placidi, X. Alcobé, V. Izquierdo-Roca, S. Kim, H. Tampo, H. Shibata, A. Pérez-Rodríguez, P. Pistor, How small amounts of Ge modify the formation pathways and crystallization of kesterites, Energy Environ. Sci. 11 (2018) 582–593, https://doi.org/10.1039/c7ee02318a.

[24] C.M. Fella, A.R. Uhl, C. Hammond, I. Hermans, Y.E. Romanyuk, A.N. Tiwari, Formation mechanism of Cu2ZnSnSe4 absorber layers during selenization of solu tion deposited metal precursors, J. Alloys Compd. 567 (2013) 102–106, https://doi.org/10.1016/j.jallcom.2013.03.056.

[25] J.A. Phys, Structural, electrical, and optical properties of Ag2ZnSnSe4 for photo-detection application structural, electrical, and optical properties of Ag 2 ZnSnSe 4 for photodetection application, 025703 (2019). doi:10.1063/1.5055895.

[26] T. Gershon, K. Sardashti, Y. Seog, O. Gunawan, S. Singh, D. Bishop, A.C. Kummel, R. Haight, Acta Materialia Compositional effects in Ag 2 ZnSnSe 4 thin fi lms and photovoltaic devices, 126 (2017) 383–388. doi:10.1016/j.actamat.2017.01.003.

[27] A. You, M.A.Y. Be, I. In, Diffusion of Rb in polycrystalline Cu (In, Ga) Se2 layers and effect of Rb on solar cell parameters of Cu (In, Ga) Se2 thin-film solar cells, 165305 (2018). doi:10.1063/1.5044629.

[28] G.K. Dalapati, S. Zhuk, S. Masudy-panah, A. Kushwaha, L. Seng, V. Chellappan, V. Suresh, Z. Su, S.K. Batabyal, Impact of molybdenum out diffusion and interface quality on the performance of sputter grown CZTS based solar cells, Sci. Rep. (2017) 1–12, https://doi.org/10.1038/s41598-017-01605-7.

[29] T. Gershon, K. Sardashti, O. Gunawan, R. Mankad, S. Singh, Y.S. Lee, J.A. Ott, A. Kummel, R. Haight, Photovoltaic Device with over 5% Efficiency Based on an n-Type Ag2ZnSnSe4 Absorber, Adv. Energy Mater. 6 (2016) 1601182, , https://doi. org/10.1002/aenm.201601182.

[30] S. Yang, S. Wang, H. Liao, X. Xu, Z. Tang, X. Li, T. Wang, X. Li, D. Liu, The impact of different Ag /(Ag + Cu) ratios on the properties, J. Mater. Science. Mater. Electron. 30 (2019) 11171–11180, https://doi.org/10.1007/s10854-019-01463-1.

[31] G. Brammertz, M. Buffière, S. Oueslati, H. ElAnzeery, K. Ben Messaoud, S. Sahayaraj, C. Köble, M. Meuris, J. Poortmans, Characterization of defects in 9.7% efficient Cu2ZnSnSe4-CdS-ZnO solar cells, Appl. Phys. Lett. 103 (2013) 163904, , https://doi.org/10.1063/1.4826448.

[32] Z. Zhang, L. Yao, Y. Zhang, J. Ao, J. Bi, S. Gao, Q. Gao, M.-J. Jeng, G. Sun, Z. Zhou, Q. He, Y. Sun, Modified back contact interface of CZTSe thin film solar cells: elimination of double layer distribution in absorber layer, Adv. Sci.(n.d.)1700645-n/a. doi:10.1002/advs.201700645.

[33] S.G. Haass, M. Diethelm, M. Werner, B. Bissig, Y.E. Romanyuk, A.N. Tiwari, 11.2% efficient solution processed kesterite solar cell with a low voltage deficit, Adv. Energy Mater. 5 (2015) 1–7, https://doi.org/10.1002/aenm.201500712.